Supporting information

A flexible protective electronic skin with tunable anti-impact and thermal insulation properties for potential rescue applications

Wenhui Wang, [a] Sheng Wang, [a]* Zimu Li, [a] Jianyu Zhou, [a] Shuai Liu, [a] Tingting Xuan, [a] Junshuo Zhang [a] and Xinglong Gong [a,b]*

[a] CAS Key Laboratory of Mechanical Behavior and Design of Materials, Department of Modern Mechanics, University of Science and Technology of China, Hefei, Anhui 230027, PR China

[b] State Key Laboratory of Fire Science, University of Science and Technology of China, Hefei, Anhui, 230026, PR China

[*] Corresponding authors: Tel: 86-551-63607605; Fax: 86-551-63600419.

E-mail: gongxl@ustc.edu.cn (X. L. Gong), wsh160@ustc.edu.cn (S. Wang).

Legends for supplementary videos

Video S1. The FPES acted as a circuit temperature switch.
Video S2. The FPES acted as an intelligent gripper.
Video S3. The balls bounced after hitting the composites in free fall.
Video S4. The wine glasses and teacups underwent a 2-meter free-fall impact.
Video S5. The force-protective area was enhanced by deformation of shape memory.
Video S6. The heating and cooling processes simulated by ABAQUS.
Video S7. The heat-protective area was enhanced by deformation of shape memory.
Video S8. FPES-based integrated impact and high-temperature alarm system.

Experimental section

Materials

All chemical reagents were used as received without additional purification. Hydroxyl silicone oil, boric acid, benzoyl peroxide (BPO) and dicumyl peroxide (DCP) were purchased from Sinopharm Chemical Reagent Co., Ltd. (China). Methyl vinyl silicone rubber (VMQ) was supplied by Shenzhen Muwei Technology Co., Ltd. (China). Ethylene-vinyl acetate (EVA, 28 wt% vinyl acetate) was provided by Yuan-Cheng Plastic & Chemical Co., Ltd. (China). The 99% ultra-pure multiwalled carbon nanotubes (CNTs) were obtained from Suzhou Tan-Feng graphene Technology Co., Ltd. (China). Table salt particles were purchased from Anhui Province Salt Industry Group Co., Ltd. (China). The plain conductive cloth tape with thickness of 0.11 mm was purchased from Shenzhen Nuoyishun electronic tape shop (China). This tape was coated with highly conductive copper and nickel metal on a high-strength polyester fiber cloth, and then covered with a high-conductive acrylic self-adhesive. The wine glasses (Model: 10 ml, 009 cup) were purchased from Chongqing Bao-Xin Glass Products Co., Ltd. (China). The ceramic teacups (Model: 50 ml, Φ 8.3 cm × H 3.2 cm) were obtained from Dehua County Xi-Xi Ceramic Business Department (China).

Preparation procedures

Boric acid was incorporated into hydroxyl silicone oil at a mass ratio of 1:36, and the resulting mixture was heated at 180 °C for 1.5 hours. Subsequently, octanoic acid was added at a ratio of 250 microliters per 100 grams of silicone oil, and the mixture was heated for an additional 0.5 hours to ensure thorough mixing. After cooling to room temperature, the shear stiffening gel (SSG) was successfully synthesized (Fig. SIa).

Next, the SSG, VMQ, and BPO were homogeneously blended using a double-roll mill (Model XK-160, China) at a mass ratio of 7:3:0.4 to obtain the precursor. This precursor was then vulcanized and cooled using a high-temperature and high-pressure vulcanizer to produce the shear stiffening elastomer (SSE) (Fig. SIb).

The SSE precursor and EVA were mixed in equal proportions, followed by the addition of DCP as the crosslinking agent at a mass ratio of 0.03:1 to EVA. Subsequently, CNTs with varying mass fractions were dispersed into the mixture to form Mixture-1. In parallel, salt particles, serving as a sacrificial template, were added with a mass ratio of 4.5:1 to the mixture, resulting in Mixture-2. These mixtures were pressed into molds of 1 mm and 10 mm thicknesses, respectively, at 170 °C and 18 MPa for 30 minutes to obtain a conductive layer and foam precursor (Fig. SIc).

The foam precursor was then ultrasonically treated in water to remove the salt particles. After drying at 80 °C for 24 hours, a porous foam was obtained. Finally, due to

the existence of shear stiffening gel with self-healing properties in the composite material of conductive layer and foam layer, the flexible protective electronic skin (FPES) with a sandwich structure was manufactured by self-adhesive two conductive layers and a foam layer in a 100 °C oven for 30 minutes (Fig. SId).

To evaluate the capacitive sensing properties of FPES, we employed plain conductive cloth tape as electrical connections. The connection size diagram of the conductive tape with the conductive layer was supplemented in Fig. SII. The electrical connection area covered had an impact on sensing performance, hence the consistent connection size was maintained across all FPES. The bond between the electrical connection and the conductive layer was established through the adhesive properties of the plain conductive cloth tape. Due to the soft nature of the electrical connection, it deformed along with the conductive layer under stress. Even after repeated compressions, the bond between the conductive tape and the conductive layer remained intact, ensuring the electrical interconnection was unaffected.

Additionally, with an increase in CNT content, the resistance of the conductive layer decreased (Fig. SIII). The resistivity of CLC with 5 wt% CNT was 11.7 Ω·m. Additionally, the sensor response of conductive layers with different carbon nanotube contents under 40% compressive strain and found that the sensor response was maximized when the CNT content was 5 wt% (Fig. SIV). Taking into consideration economic factors, a carbon nanotube mass fraction of 5 wt% was ultimately used in this study.

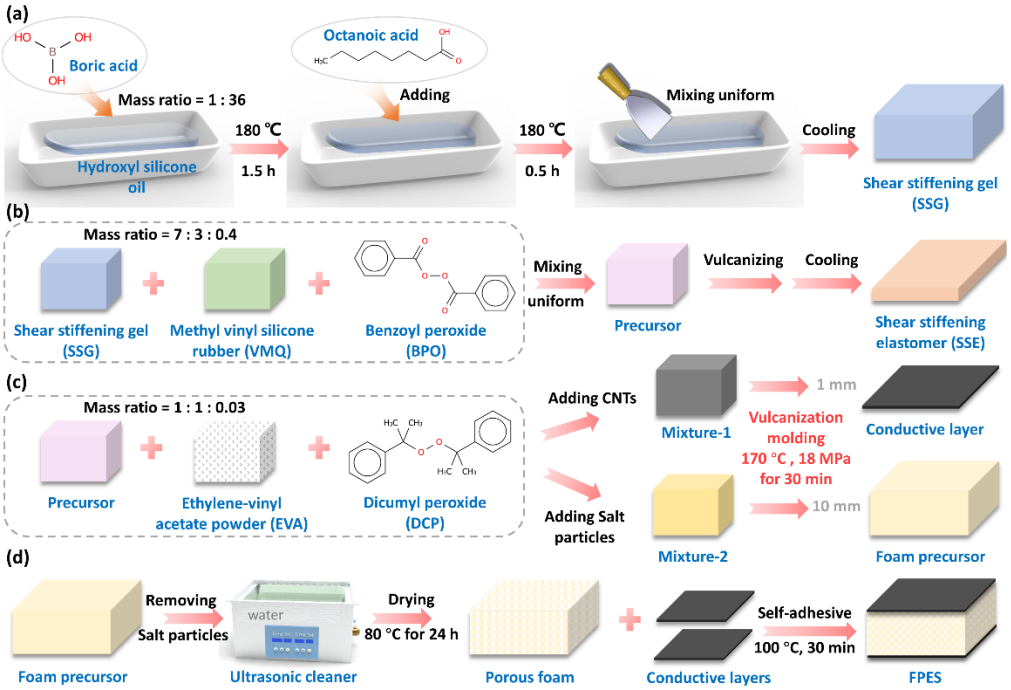

Fig. SI. The preparation flowchart of (a) SSG, (b) SSE, (c) conductive layer and foam precursor, (d) FPES.

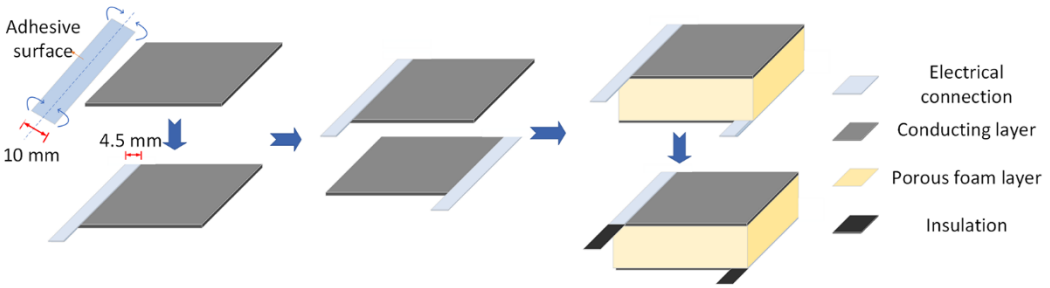

Fig. SII. The conductive tapes connection diagram.

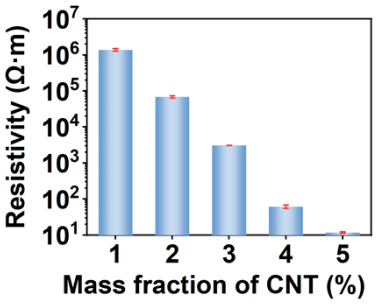

Fig. SIII. The relationship between resistivity and CNT content.

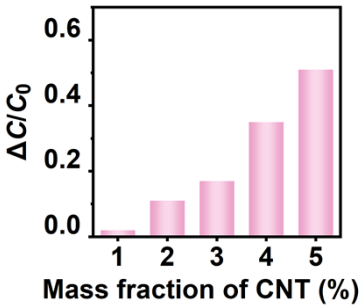

Fig. SIV. Capacitance change of FPES prepared with conductive layers with different CNT content at 40% compression.

Characterization and method

The morphological structures of the composites were characterized by field emission scanning electron microscopy (SEM, Gemini 500, Britain) and X-ray CT image processing (Dage Quadra 7, USA).

FT-IR spectra were obtained by a Fourier transform infrared spectrometer (Nicolet 8700, USA).

XRD spectra were measured by a multifunctional rotating-anode X-ray diffractometer (Smart lab, Japan).

The thermal stability was investigated by a thermogravimetric analyzer (TGA Q5000IR, USA) at a heating rate of 10 °C/min under nitrogen gas.

The temperature-dependent storage modulus was obtained using a DMA850 (TA instrument, USA) with a frequency of 1 Hz.

The frequency-dependent storage modulus and loss modulus were determined using a commercial rheometer with a parallel plate (Physica MCR 302, Anton Paar Co., Austria).

The mechanical properties of the conductive layer composite (CLC) and porous foam composite (PFC) were determined using an electronic universal testing machine (MTS, Criterion TM Model 43, USA) at a strain rate of 0.01 s^{-1}. The tensile size of CLC was 50 × 10 × 1 mm^3. The PFC with dimensions of 25 × 25 × 9 mm^3 was compressed to different strains. The total energy, denoted as E_{total}, was calculated as the integral of stress with respect to strain during the loading phase, representing the cumulative area under the stress curve in this phase. In a loading-unloading cycle, the dissipated energy, denoted as $E_{dissipated}$, was quantified by the enclosed area within the stress hysteresis loop. The dissipation ratio was defined as $E_{dissipated}$ / E_{total} (**Fig. SV**).

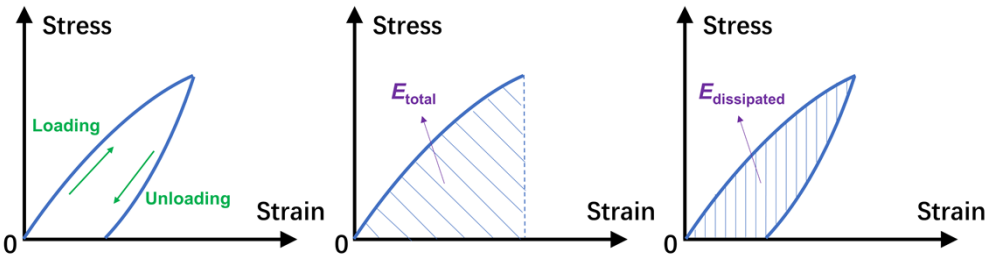

Fig. SV. Energy calculation definition diagram.

Differential scanning calorimetry (DSC) was conducted using a TA DSC-Q2000 instrument under a nitrogen atmosphere from -90 °C to 150 °C at 10 °C/min.

Thermomechanical curves of CLC and PFC were analyzed using DMA Q800 in "strain rate" mode. Briefly, a rectangular specimen with dimensions of 10 × 5 × 1 mm^3 was deformed at 75 °C followed by an isothermal hold for 5 min. The specimen was cooled to 25 °C and kept for 10 min for shape fixation. The force was then unloaded. The composite was again heated to 75 °C to trigger shape recovery. The shape fixity ratio (R_f) and shape recovery ratio (R_r) were calculated using the following equations:

$$R_f = \frac{\varepsilon}{\varepsilon_{load}} \times 100\% \quad (1)$$

$$R_r = \frac{\varepsilon - \varepsilon_{rec}}{\varepsilon} \times 100\% \quad (2)$$

where ε_{load}, ε, and ε_{rec} represent the shape memory programming strain, the strain of after unloading, and the strain after recovery, respectively.

The impact protection properties of FPES were tested using a drop hammer test

device. The impact forces of the hammer were measured using an acceleration sensor (DH131 No. 110609R, Donghuatest, China), and the residual impact forces after composite resistance were recorded using a force sensor (KD3005C No. 160114, Kedong Electronics, China). The peak force attenuation ratio was defined as:

$$\theta = 1 - \frac{F_{max}^{Sample}}{F_{max}^{Base}} \tag{3}$$

where F_{max}^{Sample} was the maximum residual impact force under sample protection, and F_{max}^{Base} was the maximum impact force directly impacting the base.

Thermal infrared images were acquired by an infrared camera (Image IR 8300, InfraTec, Germany). Thermal conductivity was measured by a thermal constants analyzer (Hot Disk TPS 2500 S, Sweden).

The capacitance of the FPES was measured using a highly sensitive LCR digital bridge (VC4092E, China), with data being stored and accessed through PC software. The minimum data access response time was 0.04 seconds to avoid delays. The relative change in capacitance ($\Delta C/C_0$) was calculated by:

$$\Delta C/C_0 = \frac{C - C_0}{C_0} \tag{4}$$

in which C_0 and C were the capacitances before and after the change, respectively.

The finite element simulation was conducted using the heat transfer (transient) step in Abaqus CAE 2020 software. The material parameters presented in **Table S3** were defined based on experimental data. These parameters include density, thermal conductivity, specific heat, and latent heat, etc. The ambient temperature was 25 °C. The bottom surface temperature of the composite was defined by the boundary condition, with temperatures set at 150 °C and 25 °C during the heating and cooling stages, respectively. The mesh types of SSE, EVA and CLC utilized the DC3D8 element, while the PFC mesh type employed the DC3D4 element.

Supplementary figures and explanatory notes

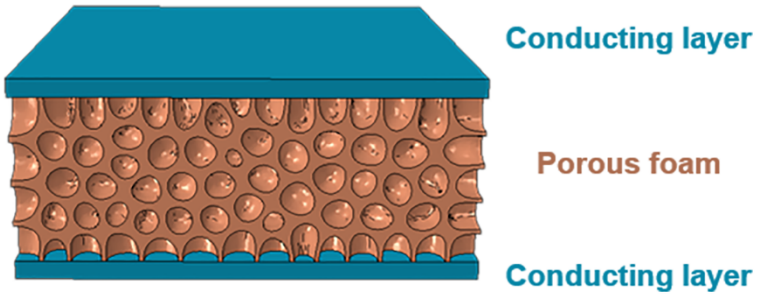

Fig. S1. The structure of FPES.

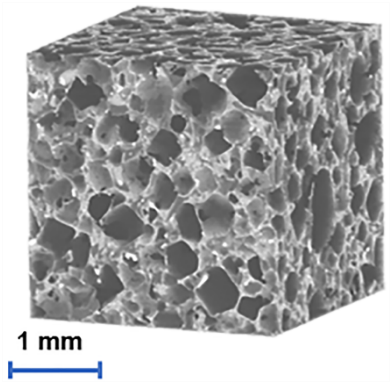

Fig. S2. A 3D reconstructed model of the porous foam.

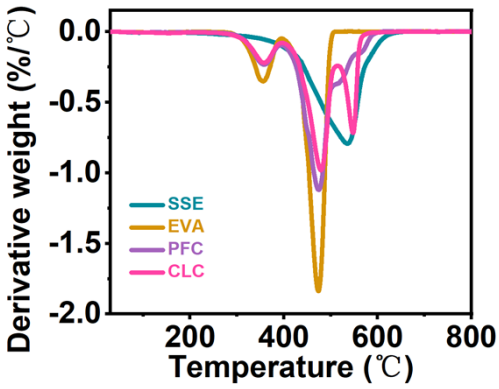

Fig. S3. DTG of SSE, EVA, PFC and CLC.

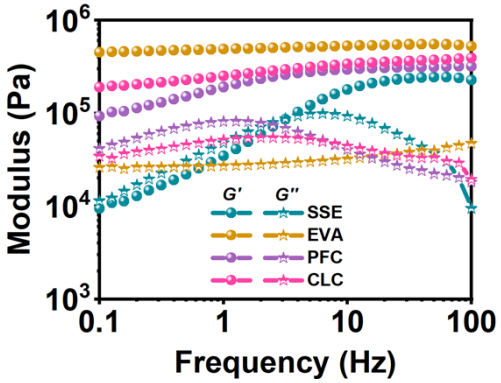

Fig. S4. Shear rheological curves of composites. The *G*' represented storage modulus and the *G*'' was loss modulus.

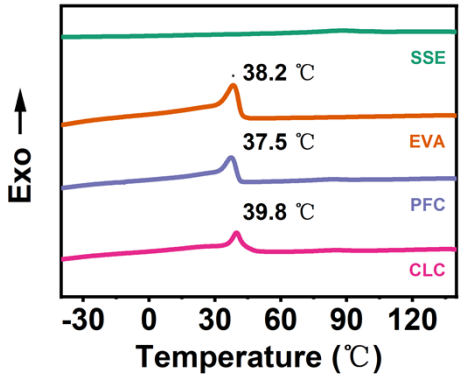

Fig. S5. DSC of the composites in the cooling phase.

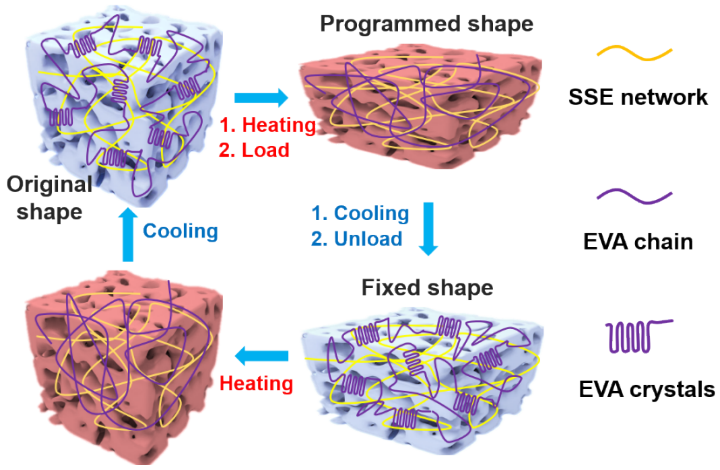

Fig. S6. The mechanism of shape memory behavior of FPES.

The shape memory performance of FPES primarily relied on the semicrystalline nature of EVA, which was thermodynamically stable at room temperature. During the shape programming process, heating caused the crystalline phases to transform into molecular chains that exhibited enhanced mobility and deformability. The load was then applied to the high-temperature FPES to obtain the desired programmed shape. Holding the load

and then cooling, these molecular chains reassembled to form crystals, resulting in the fixation of temporary shapes after unloading. Subsequent reheating above the melting temperature allowed for gradual recovery of the original conformation as reactivated molecular chains tended to release deformation energy.

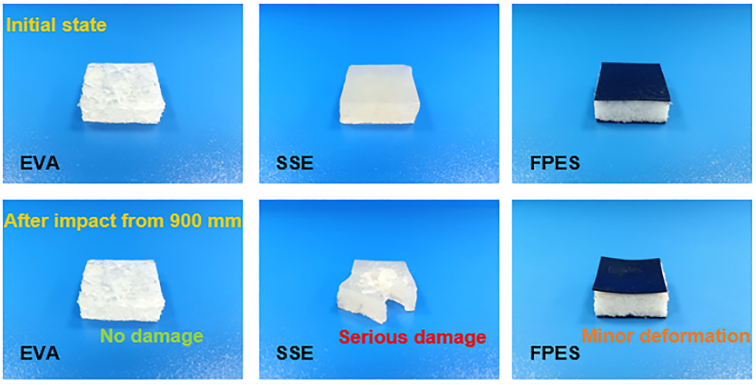

Fig. S7. Photographs before and after the impact of the SSE, EVA and FPES.

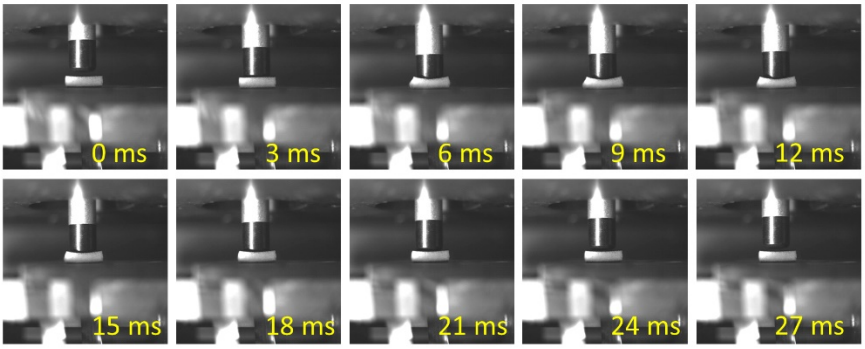

Fig. S8. Photographs of FPES subjected to a 300 mm height drop hammer impact.

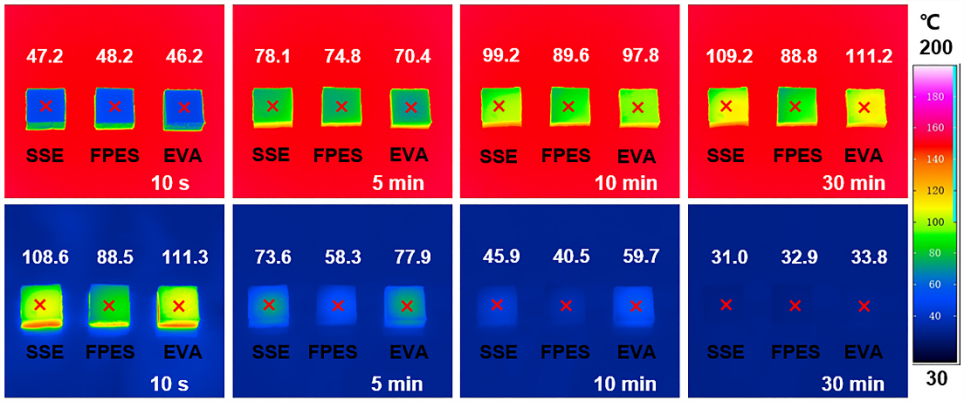

Fig. S9. Infrared temperature distribution diagram of SSE, EVA and FPES heated for 1800 s at 150 °C and then cooled for 1800 s at 25 °C.

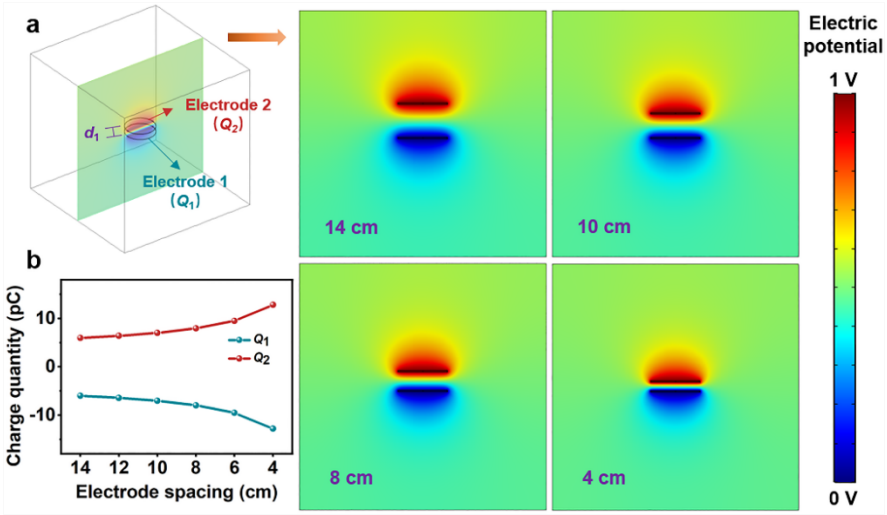

Fig. S10. Working mechanism of the FPES simulated using COMSOL. (a) Potential variation at different electrode plate distances. (b) Electrode spacing-dependent charge quantities of electrodes.

The sensing mechanism of FPES was revealed by the electrostatic module of COMSOL simulation. Two disks with a radius of 10 cm and a thickness of 0.5 cm were established as electrodes, and a cube with a size of 100 × 100 × 100 cm^3 was established as an air domain. The voltage applied to electrode 1 was adjusted to 0 V, while the voltage applied to electrode 2 was set to 1 V. The principle of charge conservation was satisfied. The distance between the two electrodes was parameterized to obtain the potential diagram of the central section (Fig. S10a). As the electrode spacing decreased, there was a gradual increase in the charge on the two electrodes (Fig. S10b). Therefore, the relationship $C=Q/U$ indicated a progressive increase in capacitance, where C represented the capacitance, Q denoted the quantity of electric charge, and U signified the voltage between the two electrodes.

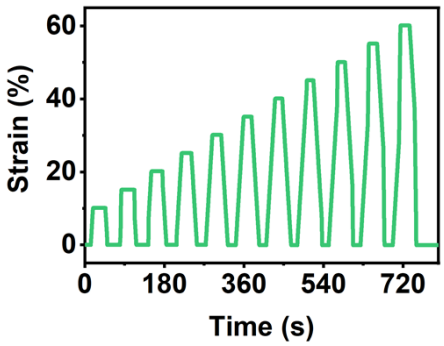

Fig. S11. Strain changing with time.

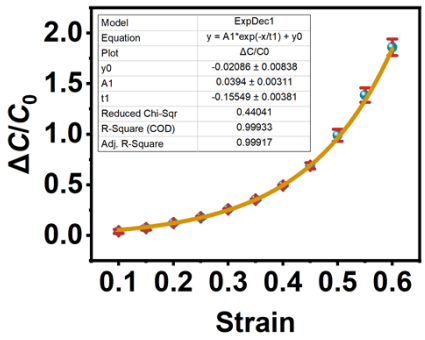

Fig. S12. Nonlinear relation between relative capacitance response and strain.

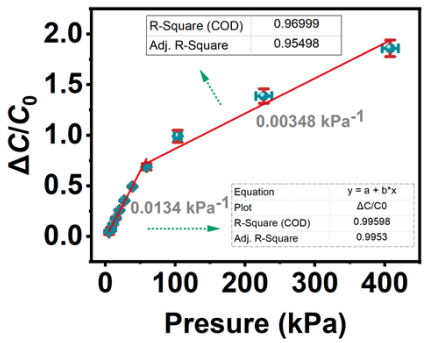

Fig. S13. Relative capacitance response with pressure.

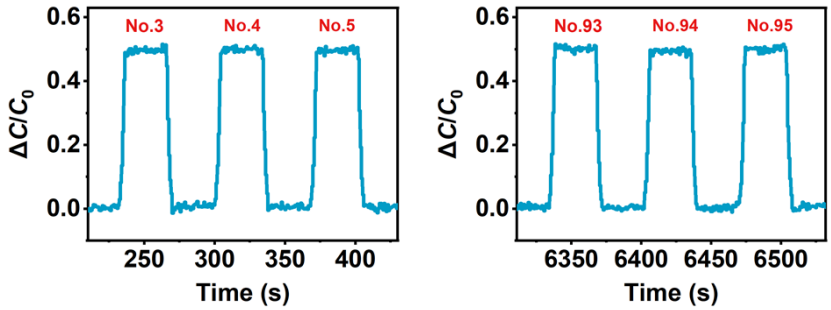

Fig. S14. Capacitance response of the FPES in cycles at a loading strain of 40%.

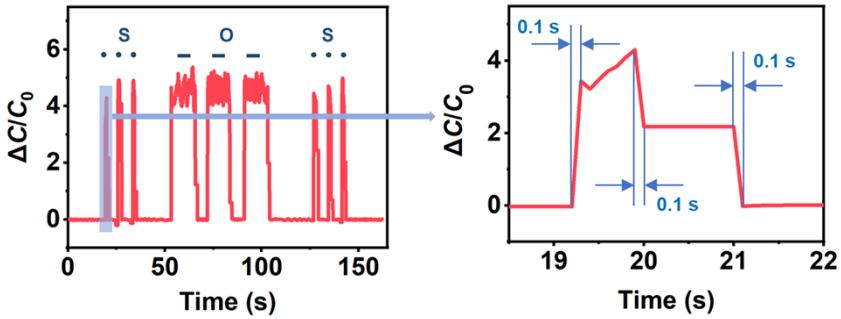

Fig. S15. Time-scale amplification of SOS Morse code pressed short or long on the FPES wrist strap.

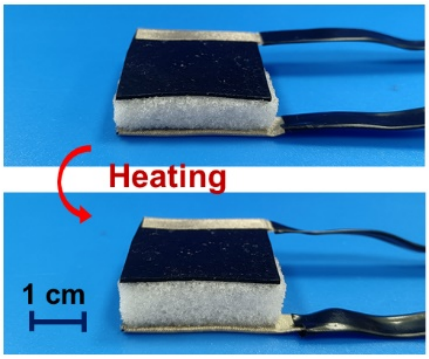

Fig. S16. Images of the temperature-dependent deformation of the CP-FPES.

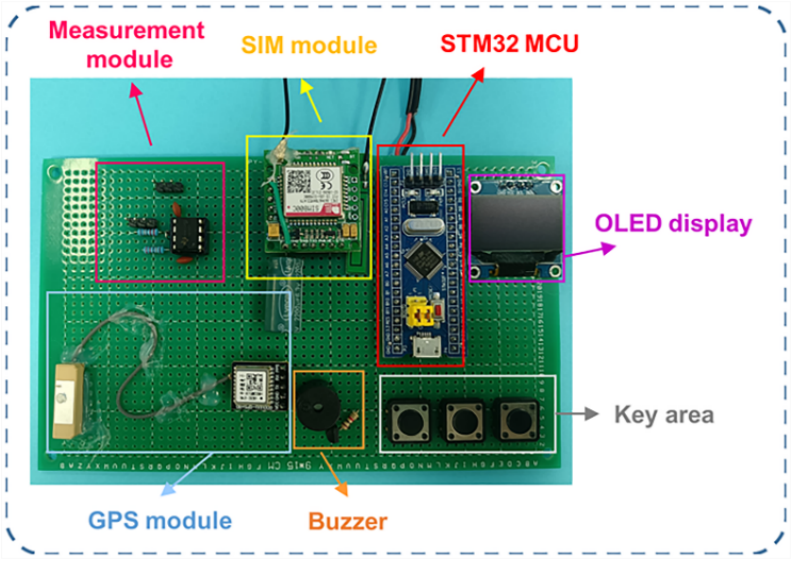

Fig. S17. Circuit diagram including the capacitance measurement module, subscriber identification module (SIM) module, MCU module (type: STM32), a global positioning system (GPS) module, a buzzer, and key modules. Note: Limited to the current GPS positioning technology, accurate location values would be obtained outdoors. Longitude and latitude coordinates were determined using the WGS84 coordinate system.

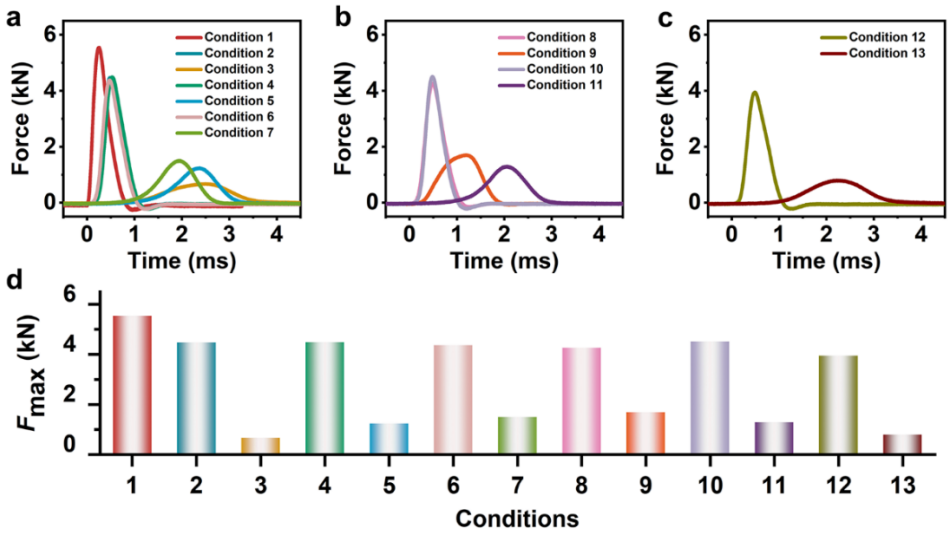

Fig. S18. Comparison of drop hammer protection properties of fabrics under different environmental conditions. (a) Residual impact forces at different temperatures. (b) Residual impact forces under varying temperature fluctuation histories. (c) Residual impact forces at relative humidity of 97% RH.

Note of experimental conditions:

Condition 1: Base equilibrated at 20 ℃;

Condition 2: Neat fabric equilibrated at 20 ℃;

Condition 3: Composite fabric equilibrated at 20 ℃;

Condition 4: Neat fabric equilibrated at 150 ℃;

Condition 5: Composite fabric equilibrated at 150 ℃;

Condition 6: Neat fabric equilibrated at 200 ℃;

Condition 7: Composite fabric equilibrated at 200 ℃;

Condition 8: Neat fabric equilibrated at 200 °C, then immersed in liquid nitrogen for 1 minute;

Condition 9: Composite fabric equilibrated at 200 °C, then immersed in liquid nitrogen for 1 minute;

Condition 10: Neat fabric equilibrated at 200 °C, then immersed in liquid nitrogen for 1 minute, followed by re-equilibration at 200 °C;

Condition 11: Composite fabric equilibrated at 200 °C, then immersed in liquid nitrogen for 1 minute, followed by re-equilibration at 200 °C;

Condition 12: Neat fabric humidified for 3 minutes (97% RH);

Condition 13: Composite fabric humidified for 3 minutes (97% RH).

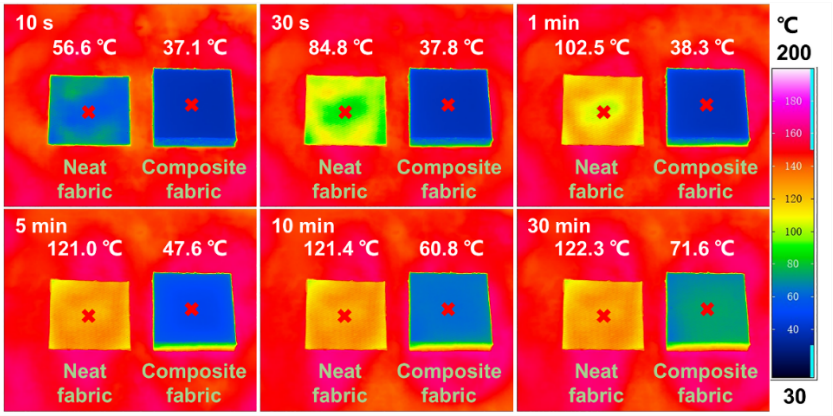

Fig. S19. The upper surface infrared temperature images of different fabrics when heated at 150 °C.

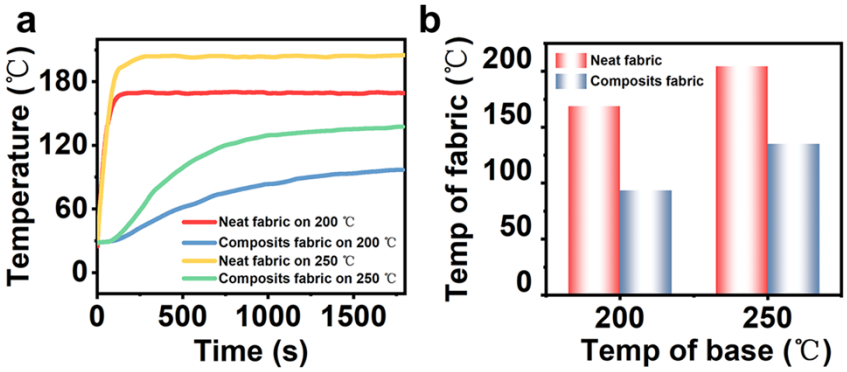

Fig S20. (a) The upper surface temperature of different fabrics when heated at 200 °C and 250 °C. (b) Comparison of upper surface temperatures of different fabrics after heating 1500 s.

Table S1. Comparisons of the density and peak force attenuation ratio.

Material	Density (g cm^{-3})	Attenuation ratio	Imapct height	Ref.
FPES	0.42	0.94	200 mm	This work
FPES	0.42	0.89	500 mm	This work
SSE	0.94	0.96	200 mm	This work
SSE	0.94	0.92	500 mm	This work
EVA	0.80	0.90	200 mm	This work
EVA	0.80	0.87	500 mm	This work
Ceramics	3.60	5.72×10^{-3}	200 mm	[1]
Steel	7.87	0.02	200 mm	[1]
PMMA	1.00	0.12	200 mm	[1]
PDMS	1.01	0.86	200 mm	[1]
Natural rubber	0.91	0.84	200 mm	[1]
PI sponge	1.49×10^{-2}	0.79	200 mm	[1]
Melamine sponge	6.52×10^{-3}	0.28	200 mm	[1]
PI-PBS	0.49	0.87	200 mm	[1]
AFSG	0.60	0.68	500 mm	[2]
F-AFSG	0.67	0.68	500 mm	[2]
PBS-10RAP	-	0.80	800 mm	[3]
PBS-15RAP	-	0.89	800 mm	[3]
LT-SSG-20%	0.66	0.91	200 mm	[4]

Note: FPES: flexible protective electronic skin; SSE: shear stiffening elastomer; EVA: ethylene-vinyl acetate; PMMA: polymethylmethacrylate; PDMS: polydimethylsiloxane; PI: polyimide; PBS: polyborosiloxane (also known as shear stiffening gel (SSG)); PI-PBS: composite consisting of viscoelastic PBS dispersively distributed in a porous polyimide matrix; AFSG: aramid nanofiber (ANF) aerogel infiltrated with SSG; F-AFSG: flame-retardant AFSG (AFSG with DOPO-HQ). PBS-10RAP: PBS with a 10% mass fraction of the reactive amphiphilic polymer (RAP); PBS-15RAP: PBS with a 15% mass fraction of the reactive amphiphilic polymer (RAP); LT-SSG-20%: lightweight and thermal-insulating shear stiffening gel with 20% mass fraction of hollow glass microspheres BR20.

Table S2. Comparisons of FPES in this work and materials in prior works.

Materials	Impact Protection	Heat Protection	Shape Memory		Sensing Capabilities		Ref.
			R_f	R_r	Type	Stimulation	
FPES	Yes	Yes	81.8 %	99.8 %	Dual response alarm sensor	Imapct and high temperature	This work
PCLE-50%	Yes	Yes	97.9 %	91.1 %	No	No	[5]
IPN	Yes	No	94.4 %	89.6 %	No	No	[6]
SMAs based tube	Yes	No	Yes but no discussion		No	No	[7]
SMA springs	No	Yes	Yes but no discussion		No	No	[8]
LM-SMF	No	Yes	--	98.9 %	No	No	[9]
SMPU/MXene paper	No	Yes	Yes but no discussion		Fire alarm sensor	High temperature	[10]
PCL-THDI	No	No	99.0 %	99.0 %	Fire alarm sensor	High temperature	[11]
PUs	No	No	≈92.5 %	≈92.5 %	Fire alarm sensor	High temperature	[12]
STF-BIPM	Yes	Yes	No	No	Impact alarm sensor	Imapct	[13]
SiCNW	Yse	Yes	No	No	Impact alarm sensor	Imapct	[14]
EASFC	Yes	Yes	No	No	Dual response alarm sensor	Imapct and temperature	[15]

Advantages and Innovations	Ref.
1. Multifunctional; 2. Shape memory dual-regulation of impact-heat protection performance; 3. Dual response alarm sensor response to impact and high temperature.	This work
1. Shape memory-induced structural deformation enhanced impact and heat protection.	[5]
1. Shape memory-induced structural deformation enhanced impact protection.	[6]
1. Shape memory-induced origami-based and kirigami-based structural deformation enhanced impact protection.	[7]
1. Shape memory-induced structural deformation enhanced heat protection.	[8]
1. Dual-regulation of electrical/thermal conductivity based on unique capacities of liquid metal and shape memory effect.	[9]
1. The fire alarm was triggered through the shape memory deformation of the flame-retardant shape memory polymer, which effectively controls the circuit switch.	[10]
1. The fire alarm was triggered through shape memory deformation of shape memory polymer, which effectively controls the electric conductivity.	[11]
1. Multifunctional; 2. Two new thermal/fire alarm devices were designed and manufactured by using shape memory PU composite material as thermal response and driving element.	[12]
Advantages and Innovations	Ref.

1. Dual-protection of impact and heat; 2. Good sensing function for impact monitoring.	[13]
1. Multifunctional sponges with lightweight, highly porous and thermally insulating features was used for monitoring structural damage or capturing impacts at a high-temperature environment.	[14]
1. Pressure and temperature sensing sensors with impact resistance and thermal insulation.	[15]

Note: FPES: flexible protective electronic skin; PCLE-50%: a heat-activated shape memory composites (PCLE) consisting of 50 wt.% polycaprolactone (PCL) and 50 wt.% shear stiffening elastomer; IPN: a thermally responsive shape memory interpenetrating polymer network consisting of polycaprolactone-based polyurethane (PUPCL) and brominated isobutylene isoprene rubber (BIIR); SMAs based tuber: shape memory alloy springs served as actuators in Origami–Kirigami Structures circular tube; SMA springs: shape memory alloy springs made of a copper-based alloy wire; LM-SMF: liquid metal shape memory polymer foam; SMPU/MXene paper: the paper consists of shape memory thermoplastic polyurethane (SMPU) and Mxene; PCL-THDI: the cross-linked network by mixing Tri-functional homopolymer of hexamethylene diisocyanate (THDI) and polycaprolactone (PCL); Pus: shape memory polyurethane (PU) composites containing graphitic-carbon fillers; STF-BIPM: shear thickening fluid reinforced biomimetic intelligent hierarchic porous material; SiCNW: SiC nanowire sponges; EASFC: Ecoflex/Aerogel/Spacer Fabric Composites.

Table S3. Material parameters in the finite element simulation.

	SSE	EVA	CLC	PFC
Density ($kg \cdot m^{-3}$)	940	800	920	840
Thermal conductivity ($W \cdot m^{-1} \cdot K^{-1}$)	0.177	0.260	0.349	0.218
Specific heat ($J \cdot kg^{-1} \cdot K^{-1}$)	1588	2685	1543	2091
Latent heat for heat stage ($J \cdot kg^{-1}$)	-	39735	16425	17343
Latent heat for cool stage ($J \cdot kg^{-1}$)	-	22882	8373	10646
Temperature range of latent heat for heat stage (°C)	-	25.0~75.0	25.0~75.0	25.0~75.0
Temperature range of latent heat for cool stage (°C)	-	30.0~46.5	33.5~50.0	31.0~43.0
Absolute zero temperature (K)	-273.15			
Stefan-Boltzmann constant ($W \cdot m^{-2} \cdot K^{-4}$)	5.67E-8			

References

[1] S. Liu, S. Wang, M. Sang, J. Zhou, T. Xuan, et al. *Chem. Eng. J.* 2023, **473**, 145214.

[2] J. Wu, Y. Wang, J. Zhang, C. Zhao, Z. Fa, et al. *Matter* 2022, **5**, 2265-2284.

[3] J. Cheng, Z. Zhang, K. Liu, C. Ma, G. Zhang. *Cell Rep. Phys. Sci.* 2023, **4**, 101289.

[4] T. Xuan, S. Wang, S. Sun, H. Deng, W. Wang, et al. *Compos. Part A Appl. Sci. Manuf.* 2023, **164**, 107312.

[5] W. Wang, S. Wang, J. Zhou, H. Deng, S. Sun, et al. *Adv. Funct. Mater.* 2023, **33**, 2212093.

[6] Q. Yu, Q. Fan, W. Chen, Y. Chen, C. Du, et al. *Chem. Eng. J.* 2024, **498**, 155410.

[7] C. Park, Y. Lee, J. Jang, M. Han. *Sensors* 2023, **23**, 2150.

[8] J. He, Y. Lu, L. Wang, N. Ma. *Materials* 2018, **11**, 1932.

[9] R. Zhao, S. Kang, C. Wu, Z. Cheng, Z. Xie, et al. *Adv. Sci.* 2023, **10**, 2205428.

[10] L. Zhang, Y. Huang, H. Dong, R. Xu, S. Jiang. *Compos. Part B Eng.* 2021, **223**, 109149.

[11] J. Jia, N. Gao, R. Li, S. Liao, S. Lyu, Y. Wang. *Chem. Eng. J.* 2022, **431**, 133285.

[12] J. Vishwakarma, S. Jaiswal, C. Dhand, R. Yeo, H. Tan, et al. *Adv. Compos. Hybrid Mater.* 2024, **7**, 203.

[13] J. Zhang, Y. Wang, J. Wu, J. Zhou, W. Wang, et al. *Chem. Eng. J.* 2023, **477**, 146939.

[14] R. Zhao, S. Kang, C. Wu, Z. Cheng, Z. Xie, et al. *Adv. Sci.* 2023, **10**, 2205428.

[15] S. Wang, J. Pu, S. Xu, Y. Tian, Q. Shu, et al. *Polymers* 2024, **16**, 1544.